POLITECNICO DI TORINO
Repository ISTITUZIONALE

# Tailored Heat-Treatment Strategies for W360 Tool Steel Produced by Directed Energy Deposition

*Original*
Tailored Heat-Treatment Strategies for W360 Tool Steel Produced by Directed Energy Deposition / Talur Chandrashekar, G., Vini, J., Rotzsche, S., Zampato, M., Finotto, C., Salmi, A., Aversa, A., Fino, P.. - In: METALS. - ISSN 2075-4701. - 16:8(2026), pp. 1-24. [10.3390/met16080848]

*Availability:*
This version is available at: 11583/3016073 since: 2026-09-29T14:06:32Z

*Publisher:*
Multidisciplinary Digital Publishing Institute (MDPI)

*Published*
DOI:10.3390/met16080848

*Terms of use:*

This article is made available under terms and conditions as specified in the corresponding bibliographic description in the repository

*Publisher copyright*

(Article begins on next page)

25 October 2026

metals

MDPI

Article

# Tailored Heat-Treatment Strategies for W360 Tool Steel Produced by Directed Energy Deposition

**Gnanesh Talur Chandrashekar [1,*], Josip Vinčić [1,2,3], Stefan Rotzsche [3], Massimo Zampato [4], Christian Finotto [4], Alessandro Salmi [5,6], Alberta Aversa [1,6] and Paolo Fino [1,6]**

1 Department of Applied Science and Technology, Politecnico di Torino, Corso Duca degli Abruzzi 24, 10129 Torino, Italy; josip.vincic@tum.de (J.V.); alberta.aversa@polito.it (A.A.); paolo.fino@polito.it (P.F.)
2 Chair of Materials Engineering of Additive Manufacturing, TUM School of Engineering and Design, Technical University of Munich, Freisinger Landstraße 52, 85748 Garching bei München, Germany
3 Munich Institute of Integrated Materials, Energy and Process Engineering (MEP), Technical University of Munich, Lichtenbergstraße 4a, 85748 Garching bei München, Germany; stefan.rotzsche@tum.de
4 EniProgetti S.p.A., Via Antonio Pacinotti 4, 30175 Venezia, Italy; massimo.zampato@eni.com (M.Z.); christian.finotto@eni.com (C.F.)
5 Department of Management and Production Engineering, Politecnico di Torino, Corso Duca degli Abruzzi 24, 10129 Torino, Italy; alessandro.salmi@polito.it
6 Interdipartimental Centre of Integrated Additive Manufacturing (IAM@PoliTO), Politecnico di Torino, Corso Castelfidardo 51, 10129 Torino, Italy
* Correspondence: gnanesh.talurchandrashekar@polito.it

**Abstract**

Laser-directed energy deposition (L-DED) was used to manufacture samples of the newly developed W360 hot-work tool steel from voestalpine Böhler Edelstahl. Various heat-treatment processes, including austenitising followed by air or water-quenching and tempering, as well as direct tempering, were applied. The as-built and heat-treated conditions were characterised by optical microscopy (OM), scanning electron microscopy–energy-dispersive X-ray spectroscopy (SEM-EDS), electron backscatter diffraction (EBSD) and X-ray diffraction (XRD), while the microstructural evolution during austenitisation was investigated using a high-temperature microscope (HTM). Hardness measurements were performed to determine the material response. The as-built condition exhibited a hardness of 628 ± 12 HV with no manufacturing cracks. The highest hardness (666 ± 13 HV) was obtained after air-quenching, whereas water-quenching produced 651 ± 14 HV. The rapid cooling of water-quenching, however, led to the formation of macroscopic cracks. The lattice distortion differences identified by XRD and the kernel average misorientation values obtained from EBSD indicated differences between the air and water-quenched conditions. High hardness (622–628 HV) was retained after low-temperature direct tempering, whereas high-temperature tempering resulted in significant softening (487 ± 12 HV). These results suggest that low-temperature direct tempering is a promising post-processing treatment for L-DED W360 tool steel, although additional mechanical testing is required to confirm industrial applicability.

**Keywords:** additive manufacturing (AM); Laser-Directed Energy Deposition (L-DED); hot-work tool steel; W360; heat treatment; hardness

Check for updates

Academic Editor: Weidong Song

Received: 11 June 2026
Revised: 14 July 2026
Accepted: 20 July 2026
Published: 4 August 2026

**Copyright:** © 2026 by the authors. Licensee MDPI, Basel, Switzerland. This article is an open access article distributed under the terms and conditions of the Creative Commons Attribution (CC BY) license.

## 1. Introduction

Additive manufacturing (AM) enables the layer-by-layer fabrication of metallic components, allowing structures to be produced or modified in ways not readily achievable

with conventional subtractive or joining processes [1,2]. Among the metal AM technologies, laser-directed energy deposition (L-DED) has attracted considerable attention because it enables relatively high deposition rates and efficient material build-up by simultaneously delivering feedstock material and a focused energy source to a substrate [3,4]. A localised melt pool is produced during the deposition process and quickly solidifies to become the deposited structure. L-DED is particularly well-suited for applications that involve volume deposition, speed and repair. However, due to its comparatively low dimensional accuracy and geometric complexity, L-DED is not routinely applied for precision manufacturing applications. For this reason, L-DED is mainly used in scenarios where the components need to be repaired, refurbished or restored [4,5].

The ability to complete such repairs is especially important in metal parts that operate under harsh service environments. In many industries, including the tool industry, repeated exposure to cyclic heating and mechanical stresses creates localised wear or cracks in parts rather than general failure [5,6]. Therefore, it would be appropriate to use a repair technique to increase the life of parts by minimising material usage [7,8]. Tool steels are therefore of particular interest for L-DED-based repair applications because they are widely used in tooling systems such as forging dies, hot-forming tools, and die-casting moulds that operate under severe thermal and mechanical loading conditions [9,10]. Within this material class, hot-working tool steels are designed for elevated-temperature applications where strength, toughness, and resistance to thermal fatigue must be maintained during cyclic heating and cooling [11,12]. The alloying elements in these steels are usually chromium, molybdenum and vanadium with enough carbon to facilitate secondary hardening and high-temperature strength [13,14]. Nevertheless, these compositional aspects also present some difficulties in the process of AM since high levels of carbon equivalents and high levels of the carbide-forming elements may enhance vulnerability to cracking, the accumulation of residual stress, and microstructural heterogeneity during the rapid solidification process [15,16].

Considering all these limitations, the application of the additive manufacturing technique in the fabrication of hot-work tooling steels is not as popular, since the high heating/cooling rate associated with AM causes the inhomogeneous distribution of solutes in the solid state through microsegregation [15,17]. To date, most previous studies related to the use of AM technology for the fabrication of hot-work tooling steels were conducted on common grades, such as H11 (X37CrMoV5-1/1.2343) and H13 (X40CrMoV5-1/1.2344). Most of these previous works studied LPBF and L-DED processability, defect formation, and bulk mechanical properties; however, microstructural changes and heat-treatment behaviour have received comparatively less attention [18–20].

As solidification progresses, solute partitioning at the solid–liquid interface leads to enrichment in the remaining liquid, resulting in microsegregation within interdendritic regions [21]. Due to rapid solidification and limited time for diffusion-controlled precipitation during AM, the coarse equilibrium carbides typically observed in conventionally processed tool steels are largely suppressed or absent in the as-built condition [22,23]. Post-deposition heat treatments are therefore commonly applied to modify these non-equilibrium microstructures. Typical objectives include relieving residual stresses, promoting phase transformations, and controlling precipitation [16,23].

Recent studies have shown that the reduction in Si and V contents in these steels leads to improved thermal fatigue resistance and toughness through the suppression of carbide coarsening [24,25]. With its lower Si and V contents, W360, a variant of H13, is gaining growing industrial interest as a tooling material in applications with high thermal fatigue and softening, especially in hot-forging and die-casting operations [16]. The lower V and Si levels, however, indicate that W360 cannot be regarded as a direct metallurgical substitute for H13 tool steel. Specifically, the lower V content affects the quantity, stability

and coarsening of MC carbides during austenitisation and tempering, whereas the lower Si content influences the tempering resistance and carbide evolution [24,25].

However, the number of studies related to AM for W360 hot-work tool steel is limited, and most of them are focused on the feasibility of the process and bulk mechanical performance. For instance, Vinčić et al. [16] showed that it is possible to obtain dense W360 tool steel by L-DED and studied the microstructural changes that occurred during the conventional heat-treatment procedure, focusing on the microstructural evolution during austenitisation. Likewise, the recent studies on powder bed fusion-processed W360, including that of Zanni et al. [26], studied the high-cycle fatigue performance of LPBF-produced W360 hot-work tool steel by comparing the effects of pressure-assisted heat treatment, i.e., hot isostatic pressing (HIP), and surface finishing conditions. Their results showed that surface finishing and HIP improved the fatigue resistance, likely due to the reduction in surface and internal defects. Their study was, however, mainly focused on the effect of pressure on a conventional heat-treatment (HT) route rather than on newly developed cycles.

While the work of Vinčić et al. [16] was mainly focused on the processability of W360 produced by the L-DED and the microstructural evolution during the conventional austenitisation, the present study systematically compares conventional quenching and tempering with multiple direct tempering routes. The effects of different post-processes on the crack susceptibility, microstructural evolution, phase constitution, lattice distortion and hardness of L-DED-fabricated W360 tool steel are evaluated systematically in this study.

However, in AM steels, the conventional heat-treatment routes developed for wrought or cast materials cannot be directly transferred without any adjustment that considers the as-built microstructure, as their response is strongly influenced by the heterogeneous as-built microstructure inherited from the building process [22,23]. Consequently, modified HT processes for AM tool steels have been examined in recent studies, such as different quench, temper and sub-zero heat treatments, to improve the microstructure and mechanical properties of the material [25]. For example, Monjez et al. [27] studied the effect of two different post-processing conditions: direct double-tempered (DTT), and quenched and double-tempered (QTT) on the evolution of the microstructure and the tensile properties of LPBF H13 compared with the as-built (AB) state. The authors found that the heat-treatment process had a significant effect on the microstructure and high-temperature mechanical properties of the material. In the same way, by using optimised annealing, austenitizing/quenching and double tempering, Omidi et al. [28] devised a customised post-heat-treatment methodology to reduce the inhomogeneity in the microstructure, porosity and oxide generation, which consequently improved the mechanical properties of LPBF H13 tool steel. Similarly, Deirmina et al. [29] found that post-processing thermal treatments have a strong effect on the fracture toughness and tempering ability of additively manufactured H13 steel, and other research studies have also demonstrated strong effects of post-processing thermal treatments on the microstructure, hardness and mechanical properties of LPBF and other AM H13 tool steels [30–32]. Together, these studies highlight the increased research on advanced post-processing heat treatments for AM tool steels, and the fact that heat-treat methods that are used for conventionally manufactured steels are not directly applicable to AM materials due to their different as-built microstructures [29–33]. However, this result cannot be directly applied to W360 since the heat-treatment response will rely on the different sequences of carbide dissolution during austenitisation and carbide reprecipitation during tempering. In most cases, however, the investigations into L-DED W360 are still of a rather isolated nature, especially the ones that address the influence of austenitisation, cooling route and direct tempering on crack susceptibility, microstructural evolution, phase constitution, lattice distortion and hardness.

The effects of austenitisation, cooling rate, and direct tempering on the susceptibility to cracking, microstructure development, phase composition, lattice distortion, and hardness of W360 tool steel manufactured by L-DED have not been studied systematically. Specifically, no research to date provides a detailed comparison between conventional quenching and tempering processes and multiple direct tempering routes for L-DED-produced W360.

The present study aims to systematically compare the four direct tempering routes of conventional austenitisation followed by air- and water-quenching with those of L-DED-produced W360 tool steel. The impact of these post-processing approaches on crack susceptibility, microstructural evolution, phase constitution, lattice distortion and hardness was assessed by high-temperature microscopy, optical microscopy (OM), scanning electron microscopy with energy-dispersive spectroscopy (SEM-EDS), electron backscatter diffraction (EBSD) and X-ray diffraction (XRD).

## 2. Materials and Methods

### 2.1. Materials

The feedstock used in this work was a commercially available gas-atomised W360 hot-work tool steel powder supplied by voestalpine Böhler Edelstahl GmbH & Co. KG (Kapfenberg, Austria), a well-established producer of special steels. The manufacturer-provided chemical composition of the alloy is reported in Table 1. This powder was employed in the L-DED process to fabricate the experimental samples [21]. Eighteen cubic samples (15 mm × 15 mm × 15 mm) were produced using a Laserdyne 430 system (AltForm S.r.Ll., Turin, Italy), equipped with a fibre laser with a maximum power of 1 kW and a 2 mm laser spot diameter. Samples were built using process parameters optimised by Vinčić et al. for W360 [16] on an AISI 316L steel substrate plate, using argon (Ar) as both a carrier and shielding gas. The geometry of the selected specimen was adequate for the intended microstructural characterisation and hardness measurement. The repeatability of the experimental observations was tested by processing two specimens for each heat-treatment condition. The processing parameters are summarised in Table 2. The optimum L-DED processing parameters were previously determined by Vinčić et al. [16] and are presented here for completeness.

**Table 1.** Chemical composition of the BÖHLER W360 tool steel powder used in this study. Adapted from Ref. [16].

| Composition | C | Si | Mn | Cr | Mo | V | Fe |
|---|---|---|---|---|---|---|---|
| Wt. % | 0.50 | 0.20 | 0.25 | 4.5 | 3.0 | 0.55 | Bal |

**Table 2.** Main laser-directed energy deposition (L-DED) processing parameters used for fabrication of the W360 specimens. Adapted from Ref. [16].

| Process Parameter | Value |
|---|---|
| Laser power (P) | 800 W |
| Scan speed (v) | 450 mm/min |
| Carrier gas flow rate (VAr) | 5 L/min |
| Laser spot diameter (dl) | 2 mm |
| Hatch overlap (Ov) | 40% |
| Z increment (Δz) | 0.65 mm |

**Table 2.** *Cont.*

| Process Parameter | Value |
|---|---|
| Scanning strategy | Zig-zag with 90° rotation between successive layers |
| Substrate material | AISI 316L |
| Carrier gas | Argon (99.99% purity) |

### *2.2. Heat-Treatment Procedures*

The specimens were subjected to different HT procedures in a tubular furnace (Nabertherm RHTC 80–710/15, Nabertherm GmbH, Lilienthal, Germany) under an argon atmosphere. The heat-treatment procedures were designed to investigate the effects of different thermal cycles on the microstructural evolution and hardness of W360. Two categories of HT were conducted: (i) a complete heat-treatment sequence involving austenitizing, quenching, and tempering (Figure 1), and (ii) direct tempering cycles performed without any prior austenitizing or quenching (Figure 2).

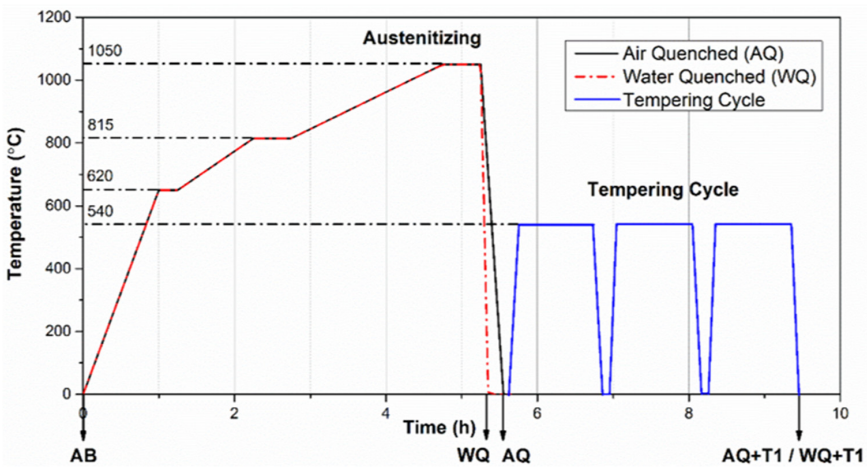


**Figure 1.** Heat-treatment cycles including austenitizing, air- and water-quenching, and triple-tempering.

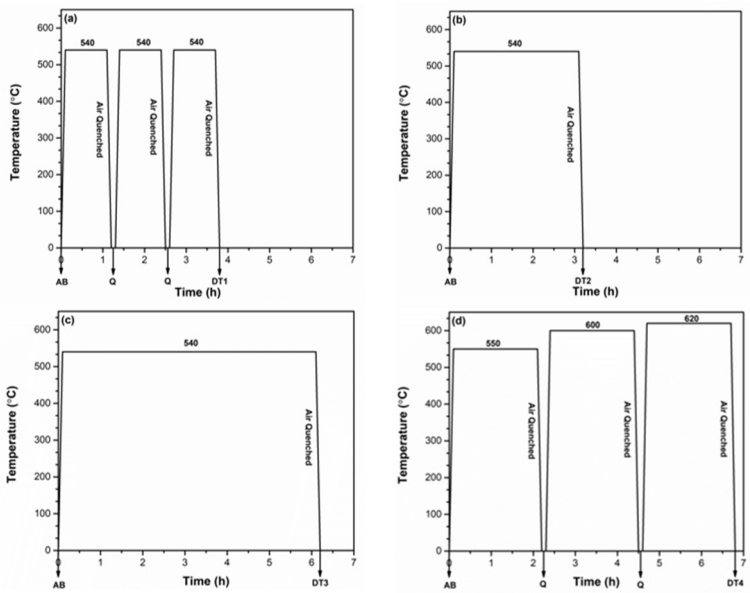


**Figure 2.** Direct tempering cycles without prior austenitizing or quenching. (**a**) DT1 cycle consisting

of three tempering cycles at 540 °C for 1 h each, with intermediate air cooling to room temperature. (**b**) DT2 cycle consisting of a single tempering treatment at 540 °C for 3 h, followed by air cooling to room temperature. (**c**) DT3 cycle consisting of a single tempering treatment at 540 °C for 6 h, followed by air cooling to room temperature. (**d**) DT4 cycle consisting of three successive tempering treatments at 550 °C, 600 °C, and 620 °C for 2 h each, with intermediate air cooling to room temperature.

The complete heat-treatment cycle applied to the L-DED-produced W360 tool steel is shown in Figure 1 and includes the preheating, austenitisation, quenching and tempering steps. The standard heat-treatment cycle was chosen as a reference cycle to be compared to the investigated heat-treatment post-processing strategies, according to the manufacturer's recommended procedure for BÖHLER W360 tool steel. Specimens were preheated in two stages at 620 °C and 815 °C to reduce thermal gradients and minimise residual stresses, which is critical for high-alloy tool steels to avoid cracking and distortion during heating [34]. The last austenitizing step was carried out at 1050 °C for 30 min to ensure homogeneity of the austenitic structure and partial dissolution and redistribution of the carbides [22].

After austenitisation, the specimens were quenched in room-temperature water (WQ), and compressed air (AQ) was used to evaluate the effect of the cooling rate [23]. No direct cooling rate measurement was made, so the comparison of the quenching conditions is thus based on the nominal quenching media. Subsequently, all specimens underwent triple-tempering at 540 °C for 1 h per cycle, with intermediate cooling to room temperature [22,35].

The direct tempering cycles applied to W360 tool steel in the as-built condition are schematised in Figure 2. The austenitisation temperature range was avoided well below the austenitisation temperature to ensure that all tempering treatments are in a diffusion-controlled range, such as recovery, stress relaxation and carbide precipitation [16,28]. This approach is well-suited for additively manufactured steels, which, thanks to the rapid cooling, are characterised by high dislocation densities and significant residual stresses induced by rapid solidification and cyclic thermal gradients [1,2].

The DT1 cycle (Figure 2a) is essentially the same as the traditional tempering cycle, but it does not involve austenitisation and quenching. The DT2 and DT3 were developed to test the influence of extended isothermal tempering (540 °C for 3 h and 6 h, respectively). This cyclic subcritical treatment could be particularly effective for AM steels because the AB material typically contains process-induced defects, such as porosity, lack-of-fusion defects, residual stresses, and microstructural heterogeneities. Repeated heating and cooling cycles may facilitate stress relaxation and microstructural stabilisation, thereby improving the material's overall performance [36,37]. Figures 2b and 2c present thermal exposures of 3 h and 6 h at 540 °C, respectively, which allow for assessment of the recovery and diffusion-controlled microstructural evolution over time. Long-term exposure at this temperature augments dislocation annihilation and carbide coarsening or redistribution within the cellular substructure, which could help to achieve gradual softening [38]. Finally, Figure 2d shows a multi-step tempering consisting of three successive stages with 2 h holding periods at progressively increasing temperatures, separated by air-cooling. These temperatures were selected to incrementally increase the severity of tempering, promoting the precipitation and evolution of the secondary alloy carbides (V-rich MC/V (C, N) and Mo-rich carbides) dominating the microstructural stability and tempering response in the hot-work tool steel secondary-hardening temperature range [39,40]. By raising the temperature, diffusion-controlled processes are increased, boosting dislocation recovery and carbide coarsening [38]. These treatments do not involve pre-austenitizing or quenching, but instead simply isolate a subcritical recovery process, which enables measurement of thermal stability and stress relaxation in the microstructure produced by DED [41].

### 2.3. In Situ Microstructure Observation During Heat Treatment

In situ microstructural observations during heat treatment were performed using a Yonekura (Yokohama, Kanagawa, Japan) SVF17SP in situ high-temperature laser scanning confocal microscope (HTM). The system combines confocal laser microscopy with a gold-coated furnace, enabling real-time observation of microstructural evolution at elevated temperatures. The system allows heating rates up to 100 K/min, and the cooling rate was up to 1800 K/min, which was made possible by the UHT module. The investigated samples had a size of $5 \times 5 \times 5$ mm$^3$ and were prepared metallographically with a surface finish of 0.06 µm silica colloidal suspension. Samples were not etched before the HTM experiments because the contrast is generated in situ by the change in surface relief and thermal grooving during heating [42]. The small size of the specimen allowed for a homogeneous temperature distribution to be obtained in the HTM experiments; however, this must be considered when comparing the in-situ observations with the bulk microstructural characterisation.

The austenitisation heat-treatment cycle illustrated in Figure 1 was simulated in the HTM experiment. The thermal cycle applied was a ramp-up at 100 K/min with isothermal holding at 620 °C for 15 min, 815 °C for 30 min and 1050 °C for 30 min.

### 2.4. Microstructural and Mechanical Characterisation

The bulk samples were sectioned in half along the build direction. These specimens were then hot-mounted in resin (diameter 40 mm). The surface of the mounted specimens was ground and polished by the usual metallographic techniques in preparation for microstructural examination. These polished surfaces were subjected to etching using 2% Nital for 60 s. The etched samples were observed with optical microscopy (LEICA DMI 5000 M, Leica Microsystems, Wetzlar, Germany) and scanning electron microscopy (SEM) (JEOL JCM-7000, JEOL Ltd., Tokyo, Japan) with energy-dispersive spectroscopy (EDS). Electron backscatter diffraction (EBSD) measurements were performed with a Tescan S900G (TESCAN ORSAY HOLDING a.s., Brno, Czech Republic) equipped with an EBSD detector (Symmetry, Oxford Instruments, Abingdon, UK). EBSD acquisitions were performed at 20 kV and 10 nA, with a step size of 0.11 µm.

The phase analysis of the cross-sectional specimens was conducted using the X-ray diffraction technique (XRD), with the help of an Empyrean diffractometer (Malvern Panalytical Ltd., Malvern, UK), in the Bragg–Brentano geometry using Cu K$\alpha$ radiation. The scan was carried out for a range of $2\theta$ between 30° and 110° with voltage and current settings of 40 kV and 40 mA, respectively [16]. The Williamson–Hall (W–H) method was used to estimate the lattice microstrain ($\varepsilon$).

Two samples were analysed for each heat-treatment condition to evaluate the repeatability of the response to the heat treatment. Detailed OM, SEM-EDS, EBSD, XRD, and hardness characterisation were performed on one representative specimen from each condition, as both processed specimens showed similar macroscopic responses after heat treatment.

Hardness measurements were carried out for a load of 9.81 N (HV) and a dwell time of 15 s with a hardness tester EVO 60A+ (QATM GmbH, Golling an der Salzach, Austria). The hardness was measured in the bulk region of the specimens, with 20 indents on each of three measurement lines parallel to the build direction (from bottom to top), to obtain hardness profiles. Indents were placed 400 µm apart and were spread out 8 mm across the distance. In the case of specimens containing cracks, hardness indentations were positioned in crack-free regions of the specimen.

## 3. Results and Discussion

The experimental results and discussion are given in this section. The experimental observations are described first, followed by interpretation and discussion with respect to

the literature in the subsections. The microstructural changes and mechanical behaviour of the L-DED-fabricated BÖHLER W360 tool steel under various heat-treatment conditions are detailed, focusing on the formation of cracks, the stability of the microstructural phases, lattice distortion and the hardness.

In a first experimental step, the effect of the cooling rate during quenching on crack formation was analysed by observing polished samples under a stereomicroscope, as shown in Figure 3. The AB specimen in Figure 3a has a relatively uniform and dense deposited structure, and there are also layer-wise solidification features, which are visible and characteristic of the L-DED process. There were no surface discontinuities or any major defects observed, which is evidence of a good metallurgical bond between the deposited layers. These observations are in line with the typical solidification characteristics of L-DED martensitic tool steels [15,43]. The AQ specimen shown in Figure 3b also exhibits a uniform appearance without visible macroscopic defects [29]. In contrast, the WQ specimen shown in Figure 3c exhibits pronounced surface-initiated cracks propagating from the top surface to the bulk material. In both WQ specimens, similar macroscopic cracking was observed, showing good repeatability of the crack propagation behaviour for the heat-treatment conditions investigated. This cracking behaviour is attributed to the severe thermal gradients imposed during WQ, which generate high tensile stresses at the surface [44,45]. In high-alloy martensitic tool steels, rapid cooling promotes martensitic transformation accompanied by volumetric expansion, which further contributes to internal stress development and crack initiation [15,46–48]. The relatively straight propagation of the observed cracks could be linked to the characteristic L-DED microstructural features (melt pool boundaries and columnar grains).

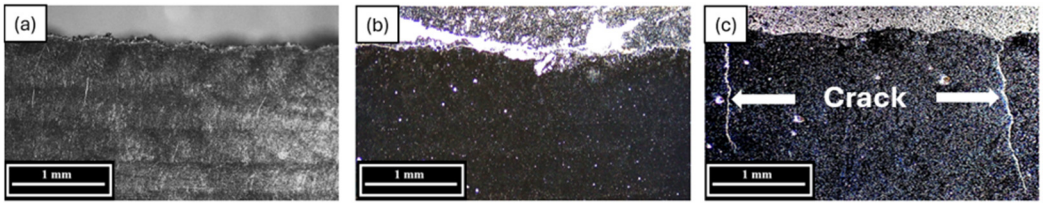


**Figure 3.** Stereo optical micrographs of the L-DED processed BÖHLER W360 tool steel after (**a**) as-built (AB), (**b**) air-quenched (AQ) and (**c**) water-quenched (WQ) processing.

The optical microscopy (OM) and scanning electron microscopy (SEM) micrographs of L-DED processed BÖHLER W360 tool steel in the as-built (AB), air-quenched (AQ), and water-quenched (WQ) conditions are shown in Figure 4. In all conditions, dark spherical features were observed and identified as process-induced pores. The porosity area fraction was estimated to be about 0.6% for the AB condition by representative image analysis (Figure 4), which means the porosity is still low enough to be below 1%. These pores are characteristic process-induced defects and are primarily associated with gas entrapment and melt pool instabilities during deposition [49].

The OM images shown in Figure 4a–c show that the cellular–dendritic structure is mainly preserved in the AB specimen and is oriented in the direction of the build. This morphology is similar to that reported for L-DED tool steels with rapid solidification behaviour [30,31]. Following quenching, the AQ and WQ specimens exhibit a comparatively more homogeneous microstructure, and the cellular solidification is not as visible after austenitisation and quenching. The WQ sample had a relatively finer microstructure with a higher cooling rate during water quenching.

The SEM-BSE micrograph of the AB sample reported in Figure 4d confirms the presence of a cellular microstructure with bright cell boundaries enriched in alloying elements. In the AB condition, alloying elements and carbide particles are predominantly segregated

along the interdendritic regions formed during rapid solidification during the L-DED process. After austenitisation, due to diffusion, the elemental segregation was reduced. In addition, bright particles are observed within the matrix in all conditions, as shown in Figure 4d–f. The representative EDS results are summarised in Table 3, where the bright areas labelled A1 contain high levels of Cr, Mo and V with respect to the matrix areas A2 [33].

**Table 3.** Representative energy-dispersive spectroscopy (EDS) point analyses of the AB, AQ, and WQ specimens. Points A1 and A2 refer to the locations identified in Figure 4. The EDS results reported here are representative results performed on several matrix areas and carbides.

| | | | **AB** | | | |
|---|---|---|---|---|---|---|
| **Region** | **Si** | **V** | **Cr** | **Mn** | **Fe** | **Mo** |
| A1 (Carbide) | 0.23 | 0.62 | 4.86 | 0.17 | 65.47 | 20.25 |
| A2 (Matrix) | 0.24 | 0.30 | 4.38 | 0.18 | 92.12 | 2.49 |
| | | | **AQ** | | | |
| **Region** | **Si** | **V** | **Cr** | **Mn** | **Fe** | **Mo** |
| A1 (Carbide) | 0.39 | 0.94 | 4.99 | 0.20 | 82.98 | 10.51 |
| A2 (Matrix) | 0.47 | 1.17 | 4.83 | 0.19 | 90.09 | 3.25 |
| | | | **WQ** | | | |
| **Region** | **Si** | **V** | **Cr** | **Mn** | **Fe** | **Mo** |
| A1 (Carbide) | 0.74 | 3.83 | 5.14 | 0.21 | 63.28 | 26.80 |
| A2 (Matrix) | 0.53 | 1.77 | 4.98 | 0.20 | 88.36 | 4.17 |

Note: Carbon was not displayed in the EDS quantification due to the inability of conventional SEM-EDS to quantify carbon in steels because it is a low-atomic-number element. A1 and A2 correspond to the EDS analysis locations shown in Figure 4, where A1 represents the carbide region and A2 represents the matrix region.

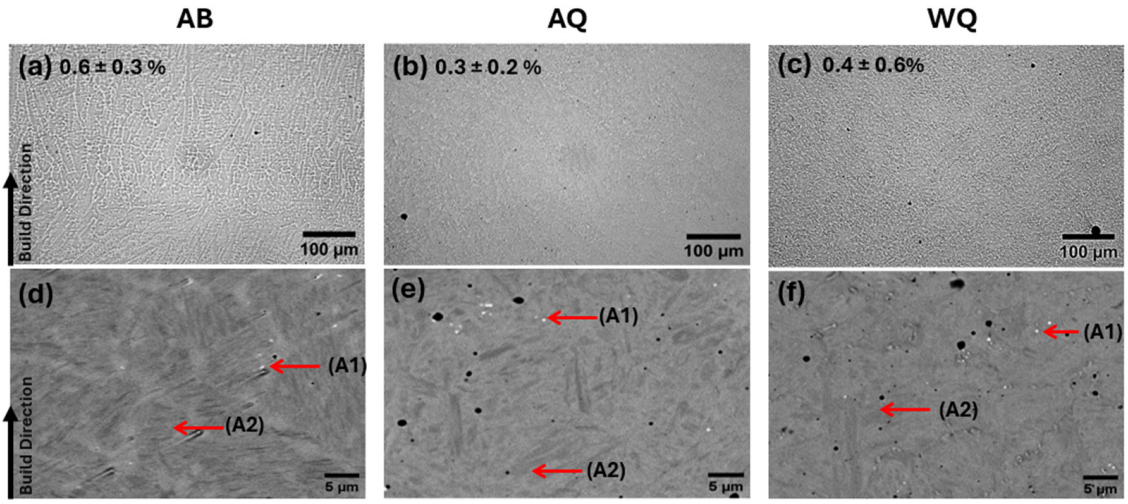


**Figure 4.** Optical microscopy (OM) and scanning electron microscopy (SEM) micrographs of L-DED processed BÖHLER W360 tool steel under different cooling conditions: (**a**) as-built (AB) (OM), (**b**) air-quenched (AQ) (OM), and (**c**) water-quenched (WQ) (OM); (**d**) AB (SEM), (**e**) AQ (SEM), and

(**f**) WQ (SEM). The build direction is indicated in (**a**) and (**d**). Scale bars: 100 µm for (**a**–**c**) and 5 µm for (**d**–**f**). The arrows labelled A1 and A2 indicate the locations selected for EDS analysis, corresponding to the carbide and matrix regions, respectively. The elemental compositions of these regions are presented in Table 3.

Analysis was carried out using the electron backscatter diffraction (EBSD) technique to identify the microstructure formed during the AB, AQ, and WQ cases, as shown in Figure 5.

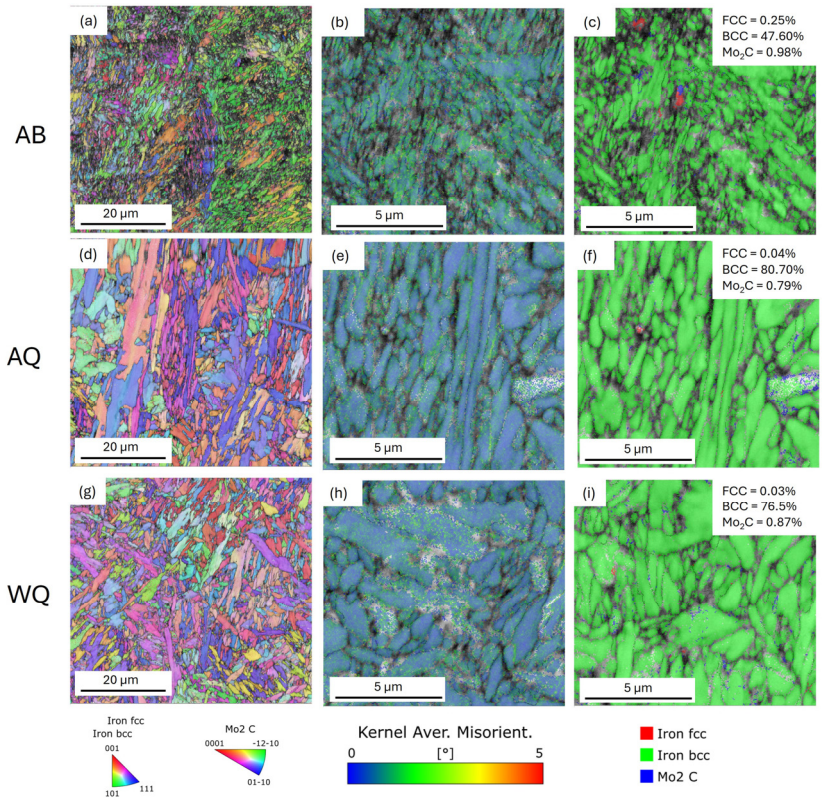


**Figure 5.** Electron backscatter diffraction (EBSD) characterisation of L-DED processed BÖHLER W360 tool steel showing the inverse pole figure (IPF) map (**a**,**d**,**g**), kernel average misorientation (KAM) maps (**b**,**e**,**h**), and phase maps (**c**,**f**,**i**) for AB, AQ and WQ conditions. Note that KAM and phase magnifications are different with respect to the inverse pole figure (IPF).

In the case of the AB condition, the inverse pole figure (IPF) map (Figure 5a) indicates that the microstructure is made of fine martensitic features with no clear preferential texture, although the presence of prior austenite grains (PAGs) can be visually recognised. The higher-magnification kernel average misorientation (KAM) map of the AB sample indicates that there are several high KAM and unindexed areas (Figure 5b). The presence of these unindexed areas is confirmed in the AB phase map reported in (Figure 5c, which reports about 50% of unindexed regions. This is probably due to the strongly distorted lattice that solidifies due to the rapid cooling. The phase map also shows that, notwithstanding the rapid cooling, the AB condition contains relatively high $Mo_2C$ (0.98%) and austenite (0.25%) contents, probably due to the repeated thermal cycling of the L-DED process and to the local chemical heterogeneities caused by the L-DED process that can probably stabilise the austenite phase. Following austenitisation, both AQ and WQ conditions still exhibit a fully martensitic microstructure with a more uniform lath-like morphology and reduced spatial heterogeneity compared to the AB condition (Figure 5a,d,g). In these IPF maps, there are no clearly discernible prior austenite grain boundaries. The reduced residual austenitic phase

fraction (~0.04%) observed in the EBSD phase maps of both quenched conditions with respect to the AB indicates that the austenitisation treatment promoted chemical homogenisation and enabled a more complete martensitic transformation during cooling [32,50]. Based on these observations, it can be concluded that the austenitisation process helped to homogenise the microstructural characteristics and decrease the heterogeneity resulting from L-DED.

Finally, AQ and WQ exhibit more uniform KAM distributions with comparable magnitudes, indicating similar geometrically necessary dislocation densities at the EBSD length scale (Figure 5b,e,h). It is noted that KAM reflects local lattice curvature and is limited in its ability to resolve absolute dislocation density and lattice strain [51].

Overall, the EBSD results indicate that the AB condition maintains the heterogeneous microstructures of the cyclic thermal history of the L-DED process, while the microstructures of AQ and WQ are similar and have the same martensitic morphologies, phase distributions and local lattice strains after austenitisation. The similarity in martensitic morphology between AQ and WQ conditions suggests that the cooling rates employed do not significantly alter the observed lath structure, which is consistent with the known influence of prior austenite grain structure on martensitic morphology [50–52].

In situ observation of austenitisation heat cycle was observed with HTM; selected frames are shown in Figure 6. The complete microstructural evolution during the heat-treatment cycle is provided in Supplementary Video S1.

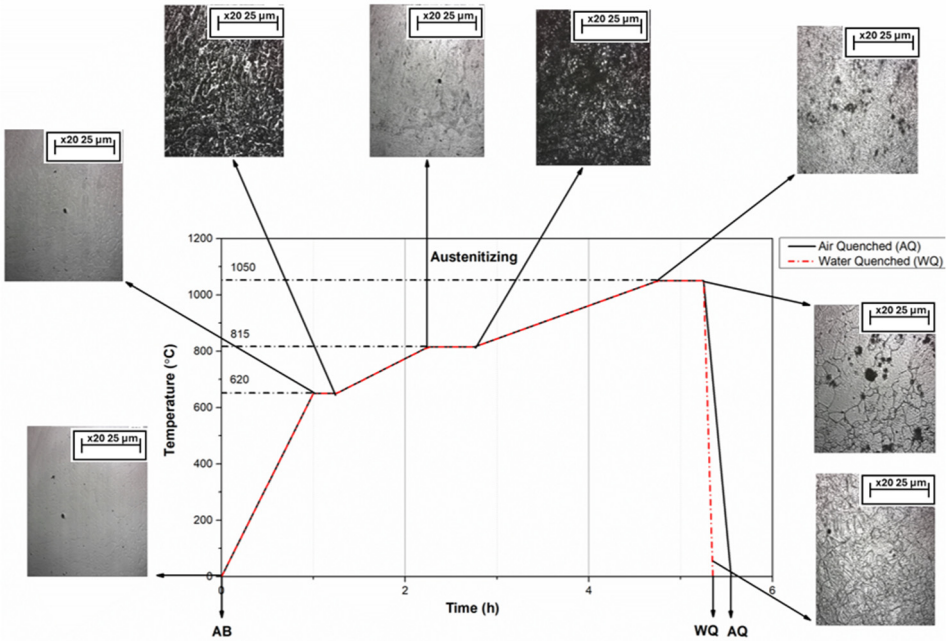


**Figure 6.** Selected frames corresponding to different stages of the heat-treatment cycle and their associated thermal profile. Scale bar: 25 µm. The complete sequence is provided in Supplementary Video S1. Video playback speed: ×20.

Supplementary Video S1, associated with Figure 6, provides direct evidence of the microstructural evolution of the L-DED BÖHLER W360 tool steel during the applied heat-treatment cycle. At room temperature, the microstructure appears relatively uniform, with visible solidification-related features and a limited number of defects or inclusions. As the temperature reaches approximately 620 °C, changes in the image contrast were observed. This observation suggests the onset of thermally induced microstructural changes and diffusion processes.

The progressive change in the microstructure was observed upon heating to 815 °C, with a decrease in the contrast of the as-built microstructural features. The holding stage at this temperature started austenitising the material and decreased the material's heterogeneity, which was introduced by the L-DED process. Further heating to 1050 °C resulted in full austenitisation and a more uniform microstructure with well-defined prior austenite grains. This microstructural change during austenitisation has been observed in additively manufactured tool steels before [53].

The effect of austenitisation and quenching rate was investigated by analysing the AB, AQ and WQ, and then a tempering treatment (T1) was applied to both the austenitised conditions, resulting in the AQ + T1 and WQ + T1. The phase evolution and mechanical response of all conditions were evaluated using X-ray diffraction (XRD) and hardness measurements.

The XRD patterns of the L-DED processed BÖHLER W360 tool steel specimens in the as-built (AB), air-quenched (AQ), water-quenched (WQ), and tempered conditions (AQ + T1 and WQ + T1) are presented in Figure 7. All diffraction patterns exhibit the characteristic α(110), α(200), α(211), and α(220) reflections associated with the martensitic BCC/BCT structure, confirming that martensite is the dominant phase irrespective of the post-processing condition. No obvious diffraction peaks in retained austenite or coarse secondary carbides were found. EBSD data showed that carbides and retained austenite content are less than about 1–3 vol.% and may not be detected under standard laboratory XRD conditions. Furthermore, very fine carbide precipitates may also not be detected depending upon their size [54,55]. The dominance of the martensitic phase suggests the high hardenability of BÖHLER W360 steel and confirms that both quenching routes after austenitisation at 1050 °C were sufficient to induce martensitic transformation.

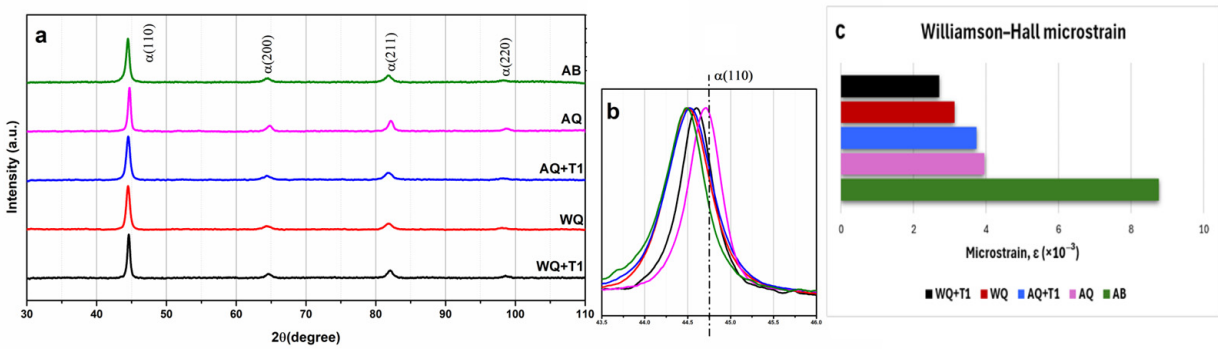


**Figure 7.** X-ray diffraction (XRD) patterns of L-DED processed BÖHLER W360 tool steel under different conditions: AB, AQ, air-quenched and triple-tempered (AQ + T1), WQ, and water-quenched and triple-tempered (WQ + T1), together with the corresponding microstrain (ε) values determined using the Williamson-Hall (W-H) method. (**a**) XRD patterns of the AB, AQ, AQ + T1, WQ, and WQ + T1 conditions, showing the diffraction peaks corresponding to the α-Fe phase. (**b**) Enlarged view of the α(110) diffraction peak, illustrating the peak shift and broadening used for microstrain analysis. (**c**) Microstrain (ε) values calculated using the Williamson-Hall (W-H) method for the different processing conditions.

A magnified view of the primary α(110) diffraction peak is shown in Figure 7b, where systematic peak shifts can be observed among the different processing conditions. The AQ condition exhibited a noticeable shift toward higher 2θ values relative to the AB condition, indicating a contraction of the martensitic lattice according to Bragg's law. This behaviour suggests the partial redistribution of carbon atoms during air-cooling and possible carbide precipitation, which reduces lattice distortion and tetragonality within the supersaturated martensitic structure. The AB condition had a non-equilibrium microstructure induced by the rapid solidification and cyclic thermal history of the L-DED process, while the AQ

condition re-austenitised all the specimens before they were AQ. These observations suggest that the observed peak shift s due to microstructural homogenisation and the redistribution of carbon and alloying elements during austenitisation. This leads to partial relaxation of the non-equilibrium lattice defects that are formed during the L-DED process, and thus a decrease in martensitic tetragonality is achieved [56]. In contrast, the WQ condition showed a peak position comparable to that of AB, indicating a similar lattice parameter. This indicates that the rapid cooling associated with water-quenching suppresses carbon diffusion and promotes retention of carbon in solid solution, thereby increasing lattice strain, tetragonality, and defect density within the martensitic matrix. The relatively small difference between the AB and WQ peak positions suggests that the lattice expansion in the WQ condition is present but limited in magnitude.

Williamson-Hall (W-H) analysis is also used to confirm these observations and quantify the lattice microstrain ($\varepsilon$) of the various heat-treatment conditions (Figure 7c). Diffraction peaks moved towards the reference $\alpha$-phase position (AQ + T1 and WQ + T1) after triple-tempering, which indicated that recovery occurred and the carbon was redistributed from supersaturated martensite to small carbide precipitates. The microstrain values, as shown in Figure 7c, decrease with T1 tempering, indicating progressive relaxation of lattice distortion and residual stresses in the martensitic matrix as observed from peak sharpening and reduction in peak shifts. No further phase transformations occurred, indicating that tempering, for the most part, retained the BCC/BCT phase constitution, but increased the stability of the martensitic matrix. As demonstrated previously, due to the rapid solidification rate and cyclic thermal history, the AB specimen is characterised by a martensitic microstructure, which results in a hardness value of about 628 ± 12 HV (Figure 8).

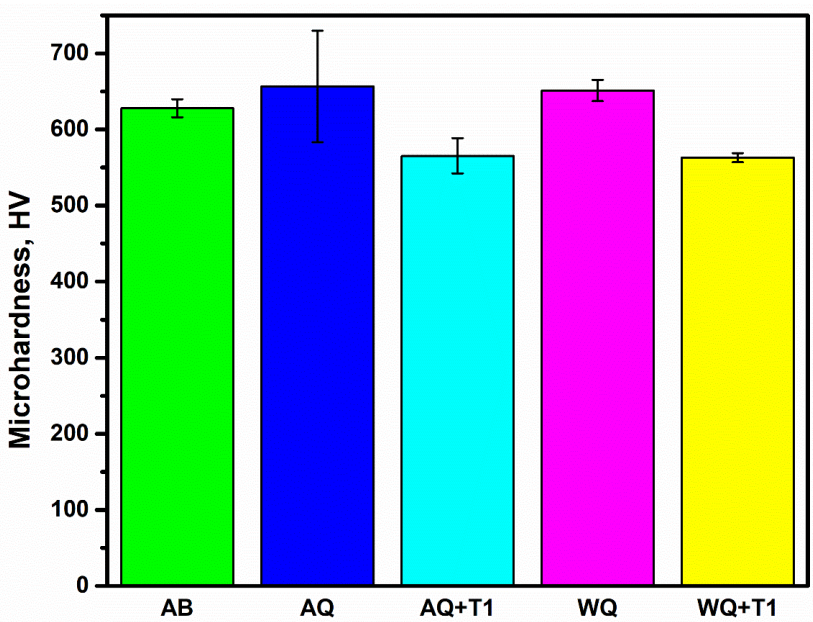


**Figure 8.** Hardness (mean ± standard deviation) of L-DED processed BÖHLER W360 tool steel under different conditions: as-built (AB), air-quenched (AQ), water-quenched (WQ), and tempered states (AQ + T1 and WQ + T1).

Following austenitisation at 1050 °C and subsequent quenching, the hardness increased to approximately 655 HV for the AQ specimen and 648 HV for the WQ specimen. Although the as-built condition was already predominantly martensitic, the increase in hardness after quenching can be attributed to the formation of fresh, untempered martensite resulting from rapid cooling after austenitisation [16,57]. Despite the higher cooling

severity of water-quenching, both AQ and WQ conditions exhibited comparable hardness values, indicating the high hardenability of Böhler W360 and its ability to achieve effective martensitic transformation under both cooling conditions [16]. The relatively larger scatter observed for the AQ condition may indicate localised microstructural heterogeneity arising from non-uniform cooling and thermal exposure during heat treatment.

After triple-tempering at 540 °C, the hardness decreased significantly to approximately 565 HV for both AQ + T1 and WQ + T1 conditions. The reduction in hardness is attributed to the tempering of martensite and the associated carbide precipitation and stress relaxation processes [57]. The comparable hardness values observed after tempering suggest that the tempering treatment effectively minimised the influence of the initial quenching condition on the final microstructural state.

Hardness profiles were obtained for AB, AQ and WQ conditions to assess the change in hardness throughout the build direction. Hardness variation was measured on all specimens, and as illustrated in Figure 9, only minor variations were found along the build direction gradient.

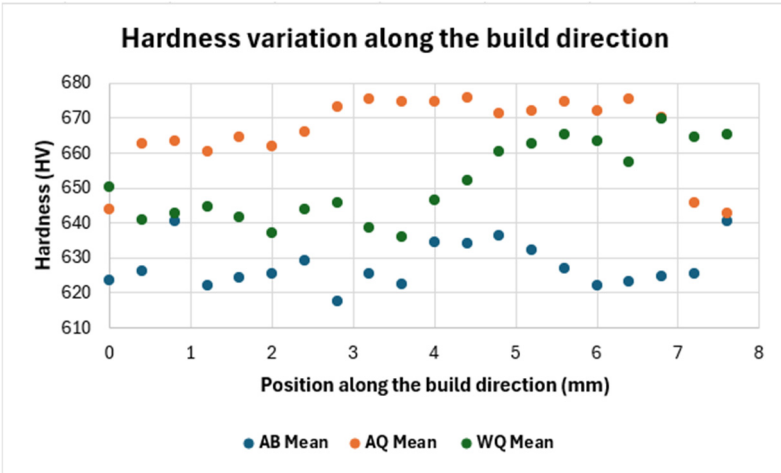


**Figure 9.** Hardness variation along the build direction for the as-built (AB), air-quenched (AQ), and water-quenched (WQ) conditions. Data points represent the average hardness measured from three parallel measurement lines at each position.

The effects of austenitisation and tempering treatments were assessed, and the feasibility of direct tempering was explored. This approach, common for AM materials, was found to be appropriate given the primarily martensitic nature of the AB condition [58]. Therefore, a series of direct tempering heat treatments was systematically studied: DT1, DT2, DT3 and DT4. Using SEM, XRD, and hardness, the microstructural evolution, phase characteristics, and mechanical response of the samples were determined.

The SEM micrographs shown in Figure 10 reveal that the L-DED processed BÖHLER W360 tool steel, subjected to different direct tempering conditions (DT1–DT4), exhibits a predominantly tempered martensitic microstructure with dispersed carbide-rich precipitated regions within the matrix. The cellular microstructural features associated with rapid solidification remain visible after direct tempering (Figure 10b–d). In addition, dark, nearly spherical features are observed throughout the microstructure and are attributed to residual porosity inherited from the L-DED process.

In all the DT conditions shown in Figure 10, the bright areas labelled D1 contain enrichment in Cr, Mo, and V, as revealed by the SEM-BSE contrast and the representative EDS point analysis for the various conditions shown in Table 4, while the darker areas labelled D2 are the Fe-rich surrounding tempered martensitic matrix. The EDS results presented in Table 4 were not statistically representative quantitative results of compositional analysis

but were performed as representative single-point analyses for qualitative identification of elemental enrichment. The enrichment of Cr, Mo and V is consistent with that of alloy carbide particles, which are produced during the tempering process in high-alloy hot-work tool steels [33,59].

**Table 4.** Representative energy-dispersive spectroscopy (EDS) point analyses of the DT specimens. Points D1 and D2 refer to the locations identified in Figure 10.

| | DT1 | | | | | | DT2 | | | | | |
|---|---|---|---|---|---|---|---|---|---|---|---|---|
| **Region** | **Si** | **V** | **Cr** | **Mn** | **Fe** | **Mo** | **Si** | **V** | **Cr** | **Mn** | **Fe** | **Mo** |
| D1 (Carbide) | 0.33 | 3.46 | 9.78 | 0.33 | 60.91 | 25.19 | 0.36 | 4.34 | 10.62 | 0.34 | 56.51 | 27.83 |
| D2 (Matrix) | 0.53 | 1.07 | 6.80 | 0.27 | 86.67 | 4.66 | 2.37 | 0.60 | 4.52 | 1.62 | 88.41 | 2.48 |
| | **DT3** | | | | | | **DT4** | | | | | |
| **Region** | **Si** | **V** | **Cr** | **Mn** | **Fe** | **Mo** | **Si** | **V** | **Cr** | **Mn** | **Fe** | **Mo** |
| D1 (Carbide) | 0.37 | 5.01 | 10.58 | 0.25 | 57.36 | 26.63 | 0.32 | 3.86 | 11.29 | 0.35 | 54.76 | 29.42 |
| D2 (Matrix) | 0.37 | 0.85 | 5.80 | 0.32 | 89.81 | 2.84 | 0.42 | 2.78 | 5.79 | 0.22 | 81.22 | 9.57 |

Note: Carbon was not included in the EDS quantification because conventional SEM-EDS cannot reliably quantify carbon in steels due to its low atomic number. D1 and D2 correspond to the EDS analysis locations indicated in Figure 10, where D1 represents the carbide region, and D2 represents the matrix region.

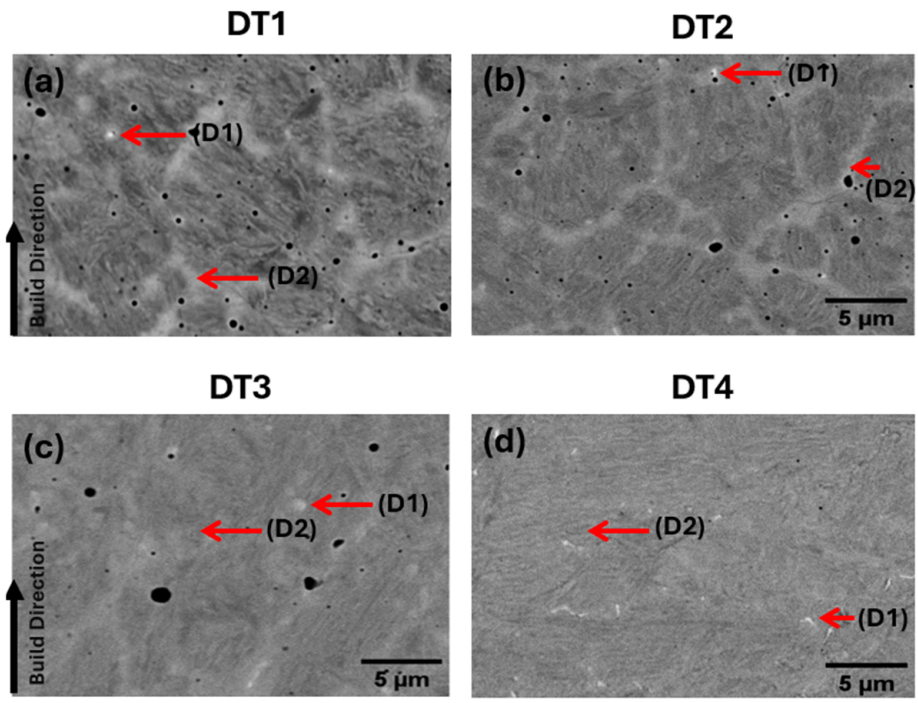


**Figure 10.** The scanning electron microscopy (SEM) images of L-DED processed Böhler W360 tool steel with different direct tempering (DT) conditions: (**a**) direct tempering cycle 1 (DT1), (**b**) direct tempering cycle 2 (DT2), (**c**) direct tempering cycle 3 (DT3), and (**d**) direct tempering cycle 4 (DT4). In (**a**,**c**), the direction of the build is shown. The arrows labelled D1 and D2 indicate the locations selected for EDS analysis, corresponding to the carbide and matrix regions, respectively. The elemental compositions of these regions are presented in Table 4.

Among the different conditions shown in Figure 10, DT1 and DT2 exhibit a comparatively higher density of fine precipitated regions distributed throughout the matrix, whereas DT3 and DT4 show a more homogeneous microstructure with reduced contrast. The precipitated regions in the DT4 condition are coarser than in the DT1-DT3 conditions, which suggests that carbide growth is greater during the higher-temperature tempering.

Also, as was seen above, the lower contrast that is found in DT4 is consistent with the diffusion, stress relaxation, and progressive recovery of the martensitic matrix during the tempering process [33,59]. The particle distribution by equivalent particle diameter in terms of volume is summarised in Figure 11, which qualitatively confirms the observations from the SEM. DT4 has a larger equivalent particle diameter, while DT2 has the finest particle size distribution of the carbide particles.

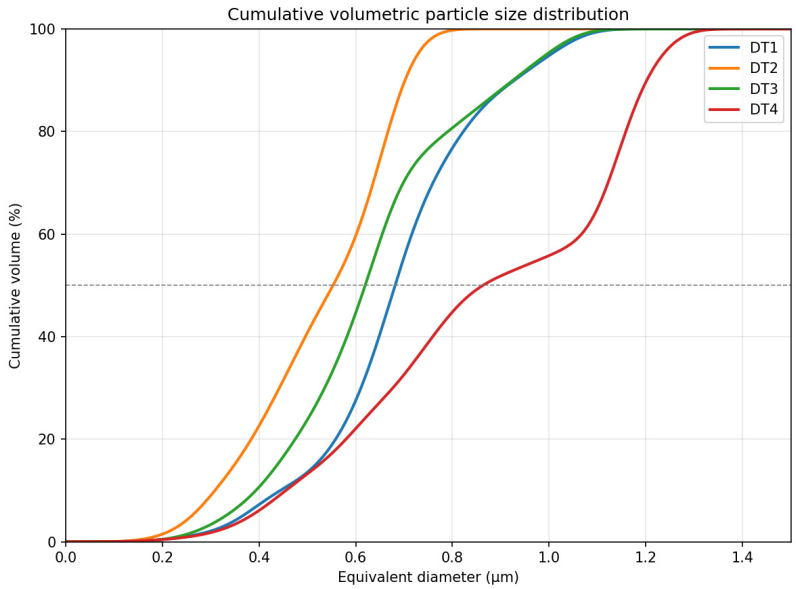


**Figure 11.** Cumulative volumetric particle size distribution of carbide particles measured from SEM micrographs for the different direct tempering (DT) conditions (DT1–DT4).

The XRD patterns for the AB and directly tempered (DT1–DT4) conditions of Böhler W360 specimens fabricated by L-DED are shown in Figure 12. The alloys W360 and conventional H13 share the same Cr-Mo-V hot-work tool steel compositional family, and the same martensitic tempering behaviour and secondary-hardening mechanisms [16,60]. The comparison with published H13 studies is therefore intended to help interpretation of the observed tempering trends rather than suggest that the metallurgical behaviour is the same. All diffraction patterns exhibit the characteristic peaks of the α-martensitic phase, indexed as α(110), α(200), α(211), and α(220), respectively, corresponding to the BCC/BCT martensitic structure typically observed in AM hot-work tool steels. No additional diffraction peaks associated with retained austenite or secondary phases were detected, indicating that the martensitic matrix remained stable throughout all direct tempering treatments.

A detailed view of the α(110) reflection, shown in Figure 12b, reveals noticeable differences in peak position among the investigated conditions. The AB condition exhibits the most shifted diffraction peak, indicating lattice distortion and residual stresses generated during rapid solidification and cyclic thermal exposure inherent in the L-DED process. Following DT, the α(110) peak progressively shifts toward the nominal α-Fe peak position, suggesting a reduction in lattice microstrain and relaxation of internal stresses through recovery mechanisms during tempering [29,61].

The Williamson-Hall (W-H) analysis can quantitatively confirm this observation by estimating the lattice microstrain (ε) for the various tempering conditions. Microstrain values for the AB condition are the highest, as shown in Figure 12c, while all the directly tempered conditions exhibit lower microstrain values, which agrees with the progressive relaxation of the lattice distortion, which corresponds to the progressive relaxation of the lattice distortion during martensitic tempering.

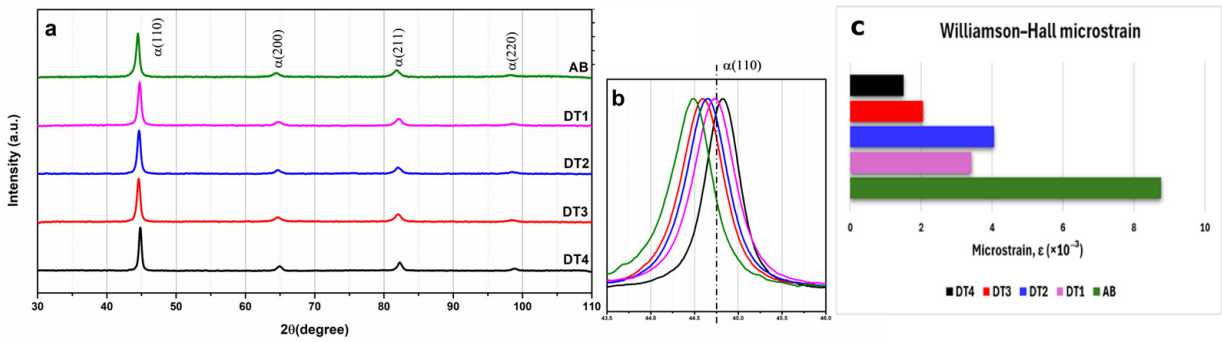


**Figure 12.** X-ray diffraction (XRD) patterns of L-DED processed BÖHLER W360 tool steel under different conditions: AB, DT1, DT2, DT3 and DT4 conditions together with the corresponding microstrain (ε) values determined using the Williamson-Hall (W-H) method. (**a**) XRD patterns of the AB, DT1, DT2, DT3, and DT4 conditions, showing the diffraction peaks corresponding to the α-Fe phase. (**b**) Enlarged view of the α(110) diffraction peak, illustrating the peak shift and peak broadening used for the Williamson-Hall microstrain analysis. (**c**) Williamson-Hall microstrain (ε) values calculated for the AB, DT1, DT2, DT3, and DT4 conditions.

The triple-stage tempering to DT1 (540 °C, 1 h + intermediate air-cooling) resulted in partial stress relief and a relatively high defect density. Progressive recovery of martensitic structure was observed with repeated heating/cooling cycles, with little change in phase constitution [29,61]. The DT2 and DT3 conditions (exposure for 3 h and 6 h at 540 °C) resulted in greater recovery because of the longer holding time. The peak position diffraction profiles observed under these conditions suggest enhanced dislocation rearrangement and annihilation, as well as the gradual relaxation of residual stresses within the martensitic matrix. The DT3 condition exhibited greater peak-narrowing, indicating increased thermal recovery and microstructural stabilisation [61]. The DT4 condition, consisting of a stepped triple-stage tempering treatment at 550 °C, 600 °C, and 620 °C for 2 h at each temperature, exhibited the most pronounced reduction in peak shift. The progressively increasing tempering temperature accelerated diffusion-controlled recovery processes and was likely associated with carbide precipitation and coarsening, resulting in more effective residual stress relaxation and reduced lattice distortion [29,61].

The measured hardness values for the AB and DT conditions are presented in Figure 13. As previously discussed, the L-DED processed BÖHLER W360 tool steel exhibited high hardness in the AB condition due to the martensitic microstructure, reaching approximately 628 ± 12 HV.

Following direct tempering, the DT1, DT2, and DT3 conditions exhibited only minor variations in hardness, remaining close to the AB condition at approximately 620–628 HV. The limited hardness reduction suggests that tempering at 540 °C, even for prolonged exposure times up to 6 h, promoted partial recovery and stress relaxation without causing substantial softening of the martensitic matrix. Compared with the AQ + T1 and WQ + T1 conditions, the directly tempered condition retained comparatively higher hardness, which may be associated with the preservation of the characteristic L-DED cellular microstructure observed in Figure 10. In contrast, the prior austenitisation treatments in AQ + T1 and WQ + T1 promote partial microstructural homogenisation and a reduction in the cellular features inherited from the AM process. These observations resulted in a tempered martensitic structure being retained with minimal microstructural coarsening.

The relatively small hardness variation between DT1, DT2, and DT3 indicates that subcritical tempering at 540 °C did not significantly alter the load-bearing martensitic framework. In contrast, the DT4 condition exhibited a pronounced hardness reduction to approximately 485 HV. The stepped tempering treatment at 550 °C, 600 °C and 620 °C

led to the significant acceleration of recovery and softening processes, which led to higher dislocation annihilation, carbide evolution and microstructural coarsening. The decrease in hardness observed is in line with improved tempering at the higher temperatures and may be related to recovery and carbide evolution [61]. This interpretation is supported by the larger carbide size observed in DT4 (Figure 11). However, further TEM analysis of the carbide would be needed to definitively determine the softening mechanism.

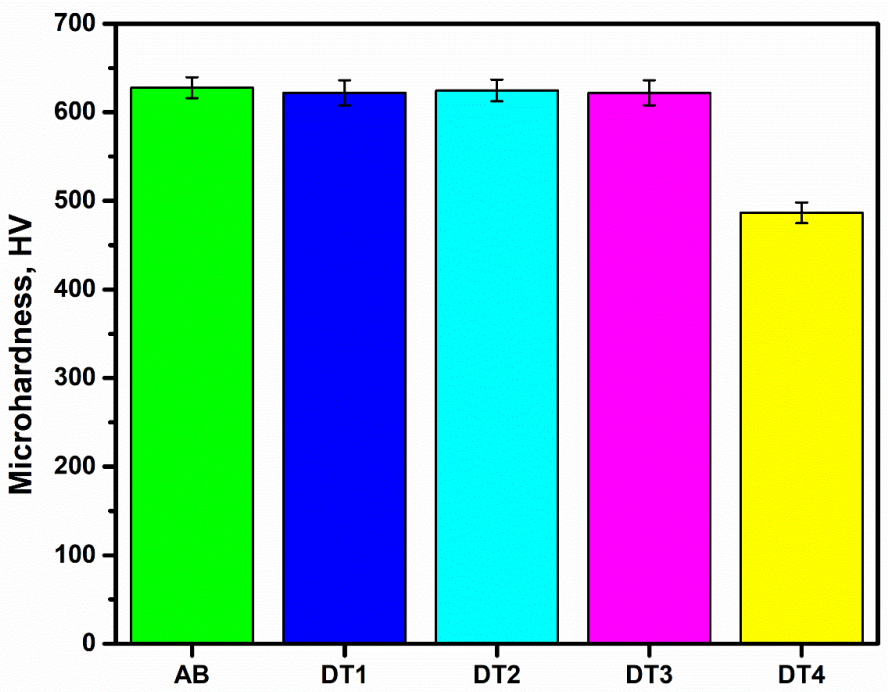


**Figure 13.** Hardness (mean ± standard deviation) of L-DED processed BÖHLER W360 tool steel under different conditions: as-built (AB) and direct tempering (DT) states (DT1, DT2, DT3 and DT4).

The retained cellular microstructure from the lower-temperature direct tempering treatments (DT1–DT3) could impact L-DED W360 tool steel service performance. Fatigue, thermal fatigue, and wear are significant damage mechanisms in hot-work tooling applications, and the microstructural heterogeneity may influence crack initiation and propagation [30,33]. These properties were not examined in the present study; however, the implications of the retained cellular microstructure for service performance deserve further investigation.

The descriptive (mean ± standard deviation) hardness results for all the investigated heat-treatment conditions are summarised in Table 5. AQ (666 ± 13 HV) and WQ (651 ± 14 HV) had the highest hardness. The hardness value of the AB condition was found to be 628 ± 12 HV; the tempered conditions DT1, DT2 and DT3 yielded similar hardness values between 622 and 625 HV. The hardness after triple-tempering after quenching was about 563–565 HV. The highest tempering temperature (DT4) had the lowest hardness level (487 ± 12 HV), which showed that the tempering treatment schedule produced a significant softening effect. The hardness data reported are descriptive measurements (mean ± standard deviation) based on repeated hardness indentations of one test specimen for each heat-treatment condition and are not intended to be statistically based comparisons of independently processed specimens.

**Table 5.** Statistical summary of the hardness measurements (HV) for all investigated heat-treatment conditions of L-DED processed BÖHLER W360 tool steel (SD = standard deviation).

| Condition | Mean ± SD |
|---|---|
| AB | 628 ± 12 |
| AQ | 666 ± 13 |
| WQ | 651 ± 14 |
| AQ + T1 | 565 ± 23 |
| WQ + T1 | 563 ± 06 |
| DT1 | 622 ± 14 |
| DT2 | 625 ± 12 |
| DT3 | 622 ± 14 |
| DT4 | 487 ± 12 |

## 4. Conclusions

The present study investigated the influence of different post-processing heat treatments on the microstructural evolution and hardness of L-DED processed BÖHLER W360 hot-work tool steel. The study revealed that the AB condition had a mostly martensitic microstructure with a hardness of 628 ± 12 HV, resulting from the fast solidification rate and the thermal history of the L-DED process. This heterogeneity was qualitatively described but not quantitatively evaluated and needs to be considered when comparing the as-built condition and post-heat-treated microstructures.

The austenitisation and quenching had a significant influence on the formation of cracks and microstructure. The WQ specimens showed the presence of visible macroscopic cracking under the investigated heat-treatment conditions, while no macroscopic cracking was observed in AQ specimens. The observed cracking is attributed to the thermally and transformation-induced stresses that are created when water is quenched rapidly. Furthermore, the SEM-EDS analysis indicated that the cooling condition affected carbide distribution and elemental segregation, whereas the EBSD analysis revealed differences in the microstructural characteristics and refinement in L-DED processed BÖHLER W360 tool steel [16,30,33].

The XRD and hardness results of the AB, AQ, WQ, AQ + T1, and WQ + T1 conditions revealed that the thermal history associated with L-DED processing, quenching routes, and subsequent tempering significantly influenced lattice distortion, residual stress state, and defect density within the martensitic matrix. The observed hardness values, peak shifts, and diffraction behaviour were consistent with the evolution of supersaturated martensite in rapidly cooled martensitic tool steels [56,62]. Triple-tempering promoted stress relaxation and microstructural stabilisation through martensite tempering and carbide precipitation while maintaining the martensitic phase constitution [16,58].

The directly tempered conditions (DT1–DT4) demonstrated that subcritical tempering treatments can effectively stabilise the AM martensitic structure without requiring prior austenitisation and quenching. In particular, the DT1–DT3 conditions retained hardness values between 622 and 625 HV, which were compared to the AB state (628 ± 12 HV), indicating good thermal stability and tempering resistance of the L-DED processed W360 steel. In contrast, the higher-temperature DT4 treatment resulted in a hardness of approximately 487 ± 12 HV, indicating significant softening consistent with enhanced tempering and recovery processes [56,58]. The quantitative particle size analysis results obtained showed that the carbide-coarsening was more pronounced in the DT4 condition, matching the SEM results.

Overall, the AQ condition (666 ± 13 HV) and direct tempering (DT1, DT2, DT3) (622–625 HV) resulted in good combinations of microstructural characteristics and hardness for the investigated processing conditions. The DT4 treatment was then much softer (487 ± 12 HV), due to the higher tempering level under the applied conditions.

This study has some limitations that should be considered when interpreting the results. The present study only considers the microstructural characterisation, XRD analysis and hardness measurements of representative specimens. Quantitative carbide size analysis, residual stress measurements, crystallographic texture evaluation, and comprehensive mechanical testing (e.g., tensile strength, wear resistance, toughness and fatigue behaviour) were beyond the scope of this study. Thus, the results of the present work are not conclusive regarding the structural performance of the L-DED W360 tool steel until further experimental testing.

The results indicate that the direct tempering process could be a post-processing method for the L-DED W360 tool steel based on the microstructural features and hardness obtained. Before direct tempering can be used as an alternative to conventional heat-treatment processes for industrial tool steel applications, further evaluation of functional properties such as tensile strength, wear resistance, toughness, fatigue behaviour, thermal softening resistance and residual stresses should be carried out.

Future research should focus on the determination of the most viable heat-treatment conditions from a large-scale industrial standpoint to provide design guidelines for L-DED W360, including comprehensive mechanical testing, comprehensive carbide characterisation, measurement of the residual stresses, and validation of the most promising heat-treatment conditions.

**Supplementary Materials:** The following supporting information can be downloaded at: https://www.mdpi.com/article/10.3390/met16080848/s1, Supplementary Video S1 shows in situ high-temperature confocal microscopy observations of the microstructural evolution of L-DED BÖHLER W360 tool steel during the applied austenitisation and quenching cycle. The video is displayed at ×20 playback speed relative to real time.

**Author Contributions:** Conceptualisation, G.T.C., J.V., and A.A.; Methodology: G.T.C., J.V., S.R., A.A. and A.S.; Software: G.T.C.; Validation: G.T.C., J.V., and A.A.; Investigation: G.T.C., J.V., S.R., A.A. and A.S.; Resources: M.Z. and C.F.; Data Curation: G.T.C.; Writing—Original Draft Preparation: G.T.C.; Writing—Review and Editing: G.T.C., J.V., S.R., M.Z., C.F., A.S., A.A., and P.F.; Visualisation: A.S.; Supervision: M.Z. and C.F.; Project Administration: P.F.; Funding Acquisition: P.F. All authors contributed equally to the conception, design, execution, and analysis of the paper. All authors have read and agreed to the published version of the manuscript.

**Funding:** This research received no external funding.

**Data Availability Statement:** The original contributions presented in this study are included in the article. Further inquiries can be directed to the corresponding author.

**Acknowledgments:** This research was carried out at Politecnico di Torino with financial assistance from Eni Progetti S.p.A. The views and findings of this document are the sole responsibility of the authors and do not necessarily reflect the official position or policies of the funding agency.

**Conflicts of Interest:** Author Massimo Zampato and Christian Finotto was employed by the company EniProgetti S.p.A. The remaining authors declare that the research was conducted in the absence of any commercial or financial relationships that could be construed as a potential conflict of interest.

## Abbreviations

The following abbreviations are used in this manuscript:

| | |
|---|---|
| AM | Additive Manufacturing |
| AB | As-Built |
| AQ | Air Quenched |
| BCC | Body-Centred Cubic |
| BCT | Body-Centred Tetragonal |
| DT | Direct Tempering Cycle |
| DT1 | Direct Tempering Cycle 1 |
| DT2 | Direct Tempering Cycle 2 |
| DT3 | Direct Tempering Cycle 3 |
| DT4 | Direct Tempering Cycle 4 |
| EBSD | Electron Backscattered Diffraction |
| EDS | Energy-Dispersive X-ray Spectroscopy |
| HT | Heat Treatment |
| HTM | High Temperature Microscope |
| IPF | Inverse Pole Figure |
| KAM | Kernel Average Misorientation |
| L-DED | Laser-Direct Energy Deposition |
| OM | Optical Microscopy |
| Q | Quenched |
| SEM | Scanning Electron Microscopy |
| T | Tempering Cycle |
| T1 | Tempering Cycle 1 |
| WQ | Water Quenched |
| XRD | X-ray Diffraction |

## References


1. DebRoy, T.; Wei, H.L.; Zuback, J.S.; Mukherjee, T.; Elmer, J.W.; Milewski, J.O.; Beese, A.M.; Wilson-Heid, A.; De, A.; Zhang, W. Additive Manufacturing of Metallic Components–Process, Structure and Properties. *Prog. Mater. Sci.* **2018**, *92*, 112–224. [CrossRef]
2. Herzog, D.; Seyda, V.; Wycisk, E.; Emmelmann, C. Additive Manufacturing of Metals. *Acta Mater.* **2016**, *117*, 371–392. [CrossRef]
3. Frazier, W.E. Metal Additive Manufacturing: A Review. *J. Mater. Eng. Perform.* **2014**, *23*, 1917–1928. [CrossRef]
4. Pinkerton, A.J. Advances in the Modeling of Laser Direct Metal Deposition. *J. Laser Appl.* **2015**, *27*, 15001. [CrossRef]
5. Graf, B.; Ammer, S.; Gumenyuk, A.; Rethmeier, M. Design of Experiments for Laser Metal Deposition in Maintenance, Repair and Overhaul Applications. *Procedia CIRP* **2013**, *11*, 245–248. [CrossRef]
6. Zenou, M.; Grainger, L. Additive Manufacturing of Metallic Materials. In *Additive Manufacturing*; Elsevier: Amsterdam, The Netherlands, 2018; pp. 53–103.
7. Bennett, J.; Garcia, D.; Kendrick, M.; Hartman, T.; Hyatt, G.; Ehmann, K.; You, F.; Cao, J. Repairing Automotive Dies with Directed Energy Deposition: Industrial Application and Life Cycle Analysis. *J. Manuf. Sci. Eng.* **2019**, *141*, 021019. [CrossRef]
8. Saboori, A.; Aversa, A.; Marchese, G.; Biamino, S.; Lombardi, M.; Fino, P. Application of Directed Energy Deposition-Based Additive Manufacturing in Repair. *Appl. Sci.* **2019**, *9*, 3316. [CrossRef]
9. Ahn, D.G. Directed Energy Deposition (DED) Process: State of the Art. *Int. J. Precis. Eng. Manuf.-Green Technol.* **2021**, *8*, 703–742. [CrossRef]
10. Girisha, V.A.; Joshi, M.M.; Kirthan, L.J.; Bharatish, A.; Hegde, R. Thermal Fatigue Analysis of H13 Steel Die Adopted in Pressure-Die-Casting Process. *Sadhana-Acad. Proc. Eng. Sci.* **2019**, *44*, 148. [CrossRef]
11. Jia, Z.X.; Liu, Y.W.; Li, J.Q.; Liu, L.J.; Li, H.L. Crack Growth Behavior at Thermal Fatigue of H13 Tool Steel Processed by Laser Surface Melting. *Int. J. Fatigue* **2015**, *78*, 61–71. [CrossRef]
12. Starling, C.M.D.; Branco, J.R.T. Thermal Fatigue of Hot Work Tool Steel with Hard Coatings. *Thin Solid Films* **1997**, *308–309*, 436–442. [CrossRef]
13. Du, K.; Lv, Z.; Fan, W.; Zhang, R.; Li, X.; Xu, L. Effect of Heat Treatment Process on Microstructure and Mechanical Properties of High-Carbon H13 Steel. *Processes* **2023**, *11*, 3239. [CrossRef]

14. Wang, H.; Li, J.; Shi, C.; Li, J.; He, B. Evolution of Carbides in H13 Steel in Heat Treatment Process. *Mater. Trans.* **2017**, *58*, 152–156. [CrossRef]
15. Platl, J.; Bodner, S.; Hofer, C.; Landefeld, A.; Leitner, H.; Turk, C.; Nielsen, M.A.; Demir, A.G.; Previtali, B.; Keckes, J.; et al. Cracking Mechanism in a Laser Powder Bed Fused Cold-Work Tool Steel: The Role of Residual Stresses, Microstructure and Local Elemental Concentrations. *Acta Mater.* **2022**, *225*, 117570. [CrossRef]
16. Vinčić, J.; Aversa, A.; Lombardi, M.; Manfredi, D. Processability and Microstructural Evolution of W360 Hot Work Tool Steel by Directed Energy Deposition. *Met. Mater. Int.* **2023**, *30*, 501–516. [CrossRef]
17. Kou, S. Solidification and Liquation Cracking Issues in Welding. *JOM* **2003**, *55*, 37–42. [CrossRef]
18. Casati, R.; Coduri, M.; Lecis, N.; Andrianopoli, C.; Vedani, M. Microstructure and Mechanical Behavior of Hot-Work Tool Steels Processed by Selective Laser Melting. *Mater. Charact.* **2018**, *137*, 50–57. [CrossRef]
19. Fonseca, E.B.; Gabriel, A.H.G.; Araújo, L.C.; Santos, P.L.L.; Campo, K.N.; Lopes, E.S.N. Assessment of Laser Power and Scan Speed Influence on Microstructural Features and Consolidation of AISI H13 Tool Steel Processed by Additive Manufacturing. *Addit. Manuf.* **2020**, *34*, 101250. [CrossRef]
20. Oliveira, A.P.; Lima, L.H.Q.R.; Felipe, B.C.A.; Bolfarini, C.; Coelho, R.T.; Gargarella, P. Effect of Microstructure and Defect Formation on the Bending Properties of Additive Manufactured H13 Tool Steel. *J. Mater. Res. Technol.* **2021**, *15*, 3598–3609. [CrossRef]
21. Wang, G.; Zhao, H.; Liang, H.; Deng, C.; Ma, W. Multi-Objective Optimisation of Process Parameters for Laser-Based Directed Energy Deposition of a Mixture of H13 and M2 Steel Powders on 4Cr5Mo2SiV1 Steel. *Virtual Phys. Prototyp.* **2024**, *19*, e2290184. [CrossRef]
22. Wang, X.; Li, C.; Zhang, Z.; Zhao, X.; Tong, D.; Yan, G.; Han, L.; Gu, J. Tailoring the Microstructure and Mechanical Properties of H13 Steel by Controlling the Pre-Precipitation of VC Carbides from Austenite. *J. Mater. Res. Technol.* **2024**, *33*, 9614–9621. [CrossRef]
23. Du, X.; Wei, Y.; Liu, X.; Zhao, W.; Liu, R. Heat Treatment Routes and Strengthening Mechanism of H13 Steel Hybrid Components Produced by Forging and Additive Manufacturing. *Mater. Sci. Eng. A* **2025**, *923*, 147762. [CrossRef]
24. Li, L.; Cai, Z.W.; Wu, X.C. Effect of Silicon on Thermal Stability of 4Cr3Mo2V Hot-Work Die Steel. *Metals* **2023**, *13*, 100. [CrossRef]
25. Zhang, Z.; Zhang, J.; Lian, Y.; Ma, M.; Zhao, C.; Ye, H.; Li, G.; Zhang, C.; Huang, J. Effects of Vanadium Content on the Carbides Transformation and Strengthening Mechanism of MPS700V Hot-Work Die Steel at Room and Elevated Temperatures. *Mater. Sci. Eng. A* **2021**, *813*, 141091. [CrossRef]
26. Zanni, M.; Di Egidio, G.; Tonelli, L.; Morri, A.; Ceschini, L. An Analysis of the Influence of Heat Treatments and Surface Finishing Conditions on the High Cycle Fatigue Behaviour of W360 Hot Work Tool Steel Produced by Powder Bed Fusion–Laser Beam. *Mater. Sci. Eng. A* **2025**, *932*, 148237. [CrossRef]
27. Monjez, M.M.; Omidi, N.; Farhadipour, P.; El Ouafi, A.; Barka, N. Influence of Different Heat Treatments on Microstructure Evolution and High-Temperature Tensile Properties of LPBF-Fabricated H13 Hot Work Steel. *Metals* **2025**, *15*, 1003. [CrossRef]
28. Omidi, N.; Houria, M.; Monjez, M.M.; Jahazi, M.; Barka, N.; Ouafi, A. El Processing Parameters Optimization for Enhanced Mechanical Strength in PBF-Ed H13 Tool Steel: Minimizing Manufacturing Defects Including Microstructural Inhomogeneity, Sub-Surface Porosities, and Oxide Formation. *Int. J. Adv. Manuf. Technol.* **2025**, *136*, 2681–2706. [CrossRef]
29. Deirmina, F.; Amirabdollahian, S.; Pellizzari, M.; Molinari, A. Effect of Different Post-Processing Thermal Treatments on the Fracture Toughness and Tempering Resistance of Additively Manufactured H13 Hot-Work Tool Steel. *Metals* **2024**, *14*, 112. [CrossRef]
30. Trojan, K.; Ocelík, V.; Čapek, J.; Čech, J.; Canelo-yubero, D.; Ganev, N.; Kolařík, K.; De Hosson, J.T.M. Microstructure and Mechanical Properties of Laser Additive Manufactured H13 Tool Steel. *Metals* **2022**, *12*, 243. [CrossRef]
31. Holzweissig, M.J.; Taube, A.; Brenne, F.; Schaper, M.; Niendorf, T. Microstructural Characterization and Mechanical Performance of Hot Work Tool Steel Processed by Selective Laser Melting. *Metall. Mater. Trans. B Process Metall. Mater. Process. Sci.* **2015**, *46*, 545–549. [CrossRef]
32. Huang, G.; Wei, K.; Zeng, X. Microstructure and Mechanical Properties of H13 Tool Steel Fabricated by High Power Laser Powder Bed Fusion. *Mater. Sci. Eng. A* **2022**, *858*, 144154. [CrossRef]
33. Deirmina, F.; Peghini, N.; AlMangour, B.; Grzesiak, D.; Pellizzari, M. Heat Treatment and Properties of a Hot Work Tool Steel Fabricated by Additive Manufacturing. *Mater. Sci. Eng. A* **2019**, *753*, 109–121. [CrossRef]
34. Zong, H.; Kang, N.; El Mansori, M. Effect of Heat Treatment on the Microstructure and Wear Behavior of AISI H13 Hot Work Tool Steel Produced via Laser Powder Bed Fusion. *Wear* **2025**, *571*, 205859. [CrossRef]
35. Ozer, A.; Ozer, M.; Atak, Ç.; Altuntas, G. The Effect of Quenching/Double Quenching and Tempering Heat Treatment Cycles on the Microstructure, Impact Energy and Hardness of AISI H13 Tool Steel. *Can. Metall. Q.* **2024**, *63*, 1138–1149. [CrossRef]
36. Chen, C.J.; Yan, K.; Qin, L.; Zhang, M.; Wang, X.; Zou, T.; Hu, Z. Effect of Heat Treatment on Microstructure and Mechanical Properties of Laser Additively Manufactured AISI H13 Tool Steel. *J. Mater. Eng. Perform.* **2017**, *26*, 5577–5589. [CrossRef]

37. Krauss, G. Tempering of Lath Martensite in Low and Medium Carbon Steels: Assessment and Challenges. *Steel Res. Int.* **2017**, *88*, 1700038. [CrossRef]
38. Luo, Y.W.; Guo, H.J.; Sun, X.L.; Guo, J.; Wang, F. Influence of Tempering Time on the Microstructure and Mechanical Properties of AISI M42 High-Speed Steel. *Metall. Mater. Trans. A* **2018**, *49*, 5976–5986. [CrossRef]
39. Ning, A.; Mao, W.; Chen, X.; Guo, H.; Guo, J. Precipitation Behavior of Carbides in H13 Hot Work Die Steel and Its Strengthening during Tempering. *Metals* **2017**, *7*, 70. [CrossRef]
40. Deirmina, F.; Amirabdollahian, S.; Lindwall, G.; Molinari, A.; Tiwari, J.K.; Hryha, E.; Pellizzari, M. On the Origin of Enhanced Tempering Resistance of the Laser Additively Manufactured Hot Work Tool Steel in the As-Built Condition. *Metall. Mater. Trans. A Phys. Metall. Mater. Sci.* **2025**, *56*, 88–110. [CrossRef]
41. Mercelis, P.; Kruth, J.P. Residual Stresses in Selective Laser Sintering and Selective Laser Melting. *Rapid Prototyp. J.* **2006**, *12*, 254–265. [CrossRef]
42. Wang, L.B.; Wan, X.L.; Hu, C.Y.; Xu, G.; Li, G.Q. High-Temperature Confocal Laser Scanning Microscopy Analysis of Phase Transformation of Steels: A Review. *J. Iron Steel Res. Int.* **2025**, *32*, 353–363. [CrossRef]
43. Cottam, R.; Wang, J.; Luzin, V. Characterization of Microstructure and Residual Stress in a 3D H13 Tool Steel Component Produced by Additive Manufacturing. *J. Mater. Res.* **2014**, *29*, 1978–1986. [CrossRef]
44. Withers, P.J.; Bhadeshia, H.K.D.H. Residual Stress. Part 1–Measurement Techniques. *Mater. Sci. Technol.* **2001**, *17*, 355–365. [CrossRef]
45. Prime, M.B. Cross-Sectional Mapping of Residual Stresses by Measuring the Surface Contour after a Cut. *J. Eng. Mater. Technol.* **2001**, *123*, 162–168. [CrossRef]
46. Olson, G.B.; Cohen, M. A General Mechanism of Martensitic Nucleation: Part I. Gen. Concepts FCC → HCP Transformation. *Metall. Trans. A* **1976**, *7*, 1897–1904. [CrossRef]
47. Patel, J.R.; Cohen, M. Criterion for the Action of Applied Stress in the Martensitic Transformation. *Acta Met.* **1953**, *1*, 531–538. [CrossRef]
48. Šolić, S.; Podgornik, B.; Leskovšek, V. The Occurrence of Quenching Cracks in High-Carbon Tool Steel Depending on the Austenitizing Temperature. *Eng. Fail. Anal.* **2018**, *92*, 140–148. [CrossRef]
49. Zhang, K.; Chen, Y.; Marussi, S.; Fan, X.; Fitzpatrick, M.; Bhagavath, S.; Majkut, M.; Lukic, B.; Jakata, K.; Rack, A.; et al. Pore Evolution Mechanisms during Directed Energy Deposition Additive Manufacturing. *Nat. Commun.* **2024**, *15*, 1715. [CrossRef] [PubMed]
50. Morito, S.; Yoshida, H.; Maki, T.; Huang, X. Effect of Block Size on the Strength of Lath Martensite in Low Carbon Steels. *Mater. Sci. Eng. A* **2006**, *438–440*, 237–240. [CrossRef]
51. Celada-Casero, C.; Sietsma, J.; Santofimia, M.J. The Role of the Austenite Grain Size in the Martensitic Transformation in Low Carbon Steels. *Mater. Des.* **2019**, *167*, 107625. [CrossRef]
52. Yoshida, H.; Takagi, S.; Sakai, S.; Morito, S.; Ohba, T. Crystallographic Analysis of Lath Martensite in Ferrite-Martensite Dual Phase Steel Sheet Annealed after Cold-Rolling. *ISIJ Int.* **2015**, *55*, 2198–2205. [CrossRef]
53. Ofner, N.; Meindlhumer, M.; Kunnas, P.; Asci, A.; Gocnik, M.; Stark, A.; Höbenreich, P.; Aumayr, C.; Wu, L.; Turk, C.; et al. In Situ Characterization of Phase and Microstructural Evolution during Multi-Step Heat Treatment of an Additively Manufac-tured Tool Steel. *J. Mater. Res. Technol.* **2025**, *37*, 2528–2538. [CrossRef]
54. Bhadeshia, H.; Honeycombe, R. Tempering of Martensite. In *Steels: Microstructure and Properties*; Butterworth-Heinemann: Oxford, UK, 2017; pp. 237–270. [CrossRef]
55. Thangadurai, P.; Lumelsky, Y.; Silverstein, M.S.; Kaplan, W.D. TEM Specimen Preparation of Semiconductor–PMMA–Metal Interfaces. *Mater. Charact.* **2008**, *59*, 1623–1629. [CrossRef]
56. Lu, Y.; Yu, H.; Sisson, R.D. The Effect of Carbon Content on the c/a Ratio of as-Quenched Martensite in Fe-C Alloys. *Mater. Sci. Eng. A* **2017**, *700*, 592–597. [CrossRef]
57. Kenevisi, M.S.; Gobber, F.S.; Fino, P.; Lombardi, M.; Bondioli, F.; Biamino, S.; Ugues, D. Tool Steels and Their Additive Manufacturing for Fabrication and Repair via PBF and DED Processes: Techniques, Challenges, and Applications. *Mater. Des.* **2025**, *258*, 114639. [CrossRef]
58. Zhao, Z.; Emanuelli, L.; Amirabdollahian, S.; Lupi, G.; Casati, R.; Deirmina, F.; Pellizzari, M. Laser-Directed Energy Deposition Additive Manufacturing of a Lean Hot Work Tool Steel: Tempering Behavior and Impact Toughness. *Mater. Sci. Eng. A* **2025**, *931*, 148220. [CrossRef]
59. Bae, K.; Moon, H.S.; Park, Y.; Jo, I.; Lee, J. Influence of Tempering Temperature and Time on Microstructure and Mechanical Properties of Additively Manufactured H13 Tool Steel. *Materials* **2022**, *15*, 8329. [CrossRef] [PubMed]
60. Williams, R.J.; Vecchiato, F.; Kelleher, J.; Wenman, M.R.; Hooper, P.A.; Davies, C.M. Effects of Heat Treatment on Residual Stresses in the Laser Powder Bed Fusion of 316L Stainless Steel: Finite Element Predictions and Neutron Diffraction Meas-urements. *J. Manuf. Process.* **2020**, *57*, 641–653. [CrossRef]

61. Saha, D.C.; Biro, E.; Gerlich, A.P.; Zhou, Y. Martensite Tempering Kinetics: Effects of Dislocation Density and Heating Rates. *Mater. Charact.* **2020**, *168*, 110564. [CrossRef]
62. Williamson, G.K.; Hall, W.H. X-Ray Line Broadening from Filed Aluminium and Wolfram. *Acta Met.* **1953**, *1*, 22–31. [CrossRef]

**Disclaimer/Publisher's Note:** The statements, opinions and data contained in all publications are solely those of the individual author(s) and contributor(s) and not of MDPI and/or the editor(s). MDPI and/or the editor(s) disclaim responsibility for any injury to people or property resulting from any ideas, methods, instructions or products referred to in the content.